

# A Local Spatio-Temporal Approach to Plane Wave Ultrasound Particle Image Velocimetry

Ecaterina Bodnariuc<sup>1</sup>, Stefania Petra<sup>1</sup>, Christoph Schnörr<sup>2</sup>, and Jason Voorneveld<sup>3</sup>

<sup>1</sup> Mathematical Imaging Group, Heidelberg University, Germany

<sup>2</sup> Image and Pattern Analysis Group, Heidelberg University, Germany

<sup>3</sup> Department of Biomedical Engineering, Erasmus MC, Thorax Center, Rotterdam, The Netherlands

**Abstract.** We present a simple and efficient approach to plane wave ultrasound particle image velocimetry (Echo PIV). Specifically, a carefully designed bank of local motion-sensitive filters is introduced, together with a method for non-linear flow parameter estimation based on time-averaged local flow estimates. The approach is validated and quantitatively assessed using both simulated and in-vitro real data, in scenarios with laminar as well as with turbulent flow.

## 1 Introduction

We are motivated by the task of estimating the instantaneous velocity of vessel blood flow using *plane wave ultrasound particle image velocimetry* (a.k.a. *Echo PIV*) [12, 20, 5]. Ultrasound techniques are used to measure blood flow in clinical applications. They enable noninvasive measurements that are applied to opaque flows. Moreover, the use of plane wave ultrasound imaging improves the temporal resolution of the signal by recording sequential ultrasound images at rates of more than 1000 frames per second over a large field of view [19].

Echo PIV is a particle image velocimetry technique developed to improve the in-plane velocity components measurements of the blood flow using clinical ultrasound machines and optical PIV image analysis algorithms [11, 15]. A schematic representation of Echo PIV is shown by Fig. 1.1.

In the presented work we restrict our attention to estimating the velocity field of pipe flows as this approximately resembles the flow in blood vessels. The velocity field of a *laminar and steady* flow (a.k.a. Poiseuille flow) is given by

$$u = u(x) = (u_1(x_2), 0)^\top, \quad u_1(x_2) = v_m \left(1 - \left(\frac{x_2}{R}\right)^2\right), \quad v_m \geq 0, \quad (1.1)$$

where  $v_m$  denotes the peak velocity of the flow in a pipe of size  $R$ , assumed to be centered at  $x_2 = 0$ . Thus, the flow has a parabolic profile, does not depend on  $x_1$ , and hence has a single degree of freedom  $v_m$ .

This smooth and laminar flow occurs at moderate Reynolds numbers. At larger Reynolds numbers the flow becomes *turbulent* and exhibits motion instability. Such flows are unsteady and irregular, yet appear steady and predictable

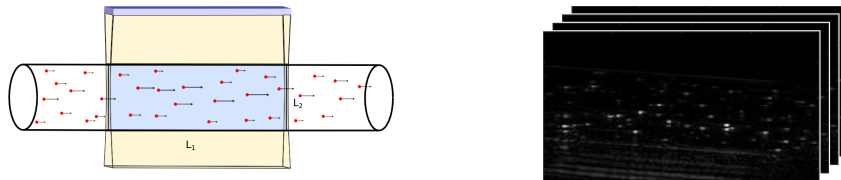


**Fig. 1.1.** Schematic representation of the plane wave ultrasound Echo PIV setup (*left*). In a rigid cylindrical tube of inner radius  $R = L_2/2$  a liquid flows that is seeded with small bubbles. A linear transducer array is placed along the tube axis and transmits a plane wave acoustic pulse into the inhomogeneous field. The same transducer then records the backscattered acoustic wave that is reflected and scattered by static tube walls and dynamic bubbles. The transmission and recording step is repeated at a rate faster than 1000 Hz. This produces images sequences with high temporal resolution (*right*) that displays speckle patterns driven by the flow.

after temporal averaging [21]. There are many empirical formulas describing the velocity profile of turbulent flow in a pipe. In this work we adopt the representation proposed in [18] in terms of the velocity field

$$u = u(x) = (u_1(x_2), 0)^\top, \quad u_1(x_2) = v_m \left(1 - \left(\frac{|x_2|}{R}\right)^{N+1}\right). \quad (1.2)$$

For  $N = 1$  we recover the parabolic velocity profile of (1.1) and for  $N > 1$  a deformed velocity profile is obtained.

A common assumption of experimental fluid dynamics [16] is that the flow has been seeded with a set of randomly located particles, also called tracer particles, that follow the flow dynamics. Motion is estimated via the displacement of these tracer particles. In the present work, we focus on speckle patterns originating from microbubbles that are driven by laminar or turbulent pipe flow (Fig. 1.1).

**Related Work and Contribution.** Research on plane wave Echo PIV is concerned with (i) image reconstruction and (ii) motion estimation. We only focus on (ii) motion estimation. For recent work on (i) image reconstruction based on inverse scattering, we refer to [4] and references therein.

We present the *design* of a spatio-temporal filter bank for local motion extraction from plane wave Echo PIV image sequences. The motivation is threefold:

1. The high frame rates of plane wave ultrasound imaging lead to displacements that enable the application of *differential* motion estimation techniques [2].
2. The flow model (1.2) corresponds to a specific geometry of the spectral support of the image sequence in the Fourier domain. This motivates a careful design of a filter bank in order to properly “discretize” the Fourier domain, while forming a partition of unity to achieve uniform motion sensitivity.
3. While correlation technique for motion estimation prevail in PIV applications [16], alternative techniques from computer vision have proven to be useful as well [10]. Our present work constitutes a first step of adapting such techniques to the specific domain of Echo PIV.

The design of orientation- and motion-sensitive local filters has a long tradition in image processing and computer vision [9, 6, 7], in models of early natural vision [1, 14] and in the wavelet community [13, 17]. Our goal is a proper discretization of a half-space in the spatio-temporal Fourier domain (only relevant for real-valued signals) in terms of a collection of motion-sensitive filters whose spectral supports form a partition of unity. This requirement rules out Gabor filters in favour of log-Normal filters that behave more conveniently in the spectral domain (cf. [14]), and wavelet filter banks [13] due to the lack of rotational invariance.

Our filter bank is presented in Section 2. Section 3 summarizes established techniques for local motion estimation based on the phase-shifts of filter responses. Experimental results using the filter bank are discussed in Section 4: computer-generated ground-truth sequences illustrate properties of the filter bank; flow and flow model parameter estimates for real in-vitro data, both in laminar and in turbulent flow scenarios, validate our approach.

The integration of our local approach into a more advanced non-local variational scheme is beyond the scope of this paper and will be reported elsewhere.

## 2 Spatio-Temporal Filter Bank

We detail the design of a bank of spatio-temporal filters. The representation in spherical coordinates enables to illustrate the radial dependency in 1D and the two angular dependencies in 2D and 3D, respectively.

**Design Criteria.** The major aspects are:

- Self-similar parametrization in terms of a sequence of center frequencies, such that all filters form a partition of unity of the frequency interval  $[\frac{\pi}{16}, \frac{\pi}{4}]$ . Structures that generate lower frequencies are not relevant in our scenario, and the dependency on the global mean is removed. Frequencies larger than  $\frac{\pi}{2}$  are regarded as noise.
- All filters form a partition of unity of both angular ranges. We thereby ignore an arbitrary half-space due to the symmetry of real signals in the Fourier domain.
- The coordinate system is oriented so that the second angular dependency enables to control the selectivity with respect to the flow velocities parametrized by  $x_2$  in (1.2), including the peak velocity  $v_m$  at  $x_2 = 0$ .

**The Log-Normal Filters.** The transfer function of the one-dimensional log-normal filter with center frequency  $\omega_i \geq 0$  and width  $\sigma_i \geq 0$  is given by

$$\hat{g}_i(\omega) = \frac{1}{C(\sigma_i)} \frac{\omega_i}{\omega} \exp \left[ -\frac{1}{2} \left( \frac{\log(\frac{\omega}{\omega_i})}{\sigma_i} \right)^2 \right], \quad \omega \geq 0, \quad (2.1)$$

where  $C(\sigma_i) = \sqrt{2\pi}\sigma_i$ . The norm of each filter is

$$\|\hat{g}_i\|_{L^1(\mathbb{R}_+)} = \omega_i. \quad (2.2)$$

The set of center frequencies and frequency widths

$$\omega_i = c^{(i-1)}\omega_1, \quad \sigma_i^2 = \log \frac{\omega_{i+1}}{\omega_i} = \log c, \quad c > 1, \quad i = 1, 2, \dots \quad (2.3)$$

defines a filter bank  $\{\hat{g}_i(\omega)\}_{i \geq 1}$ , given by (2.1) such that  $\hat{g}_{i+1}(\omega) = \frac{\omega}{\sqrt{\omega_i \omega_{i+1}}} \hat{g}_i(\omega)$ . These parameters are also used below in the case of 2- and 3-dimensional filter banks.

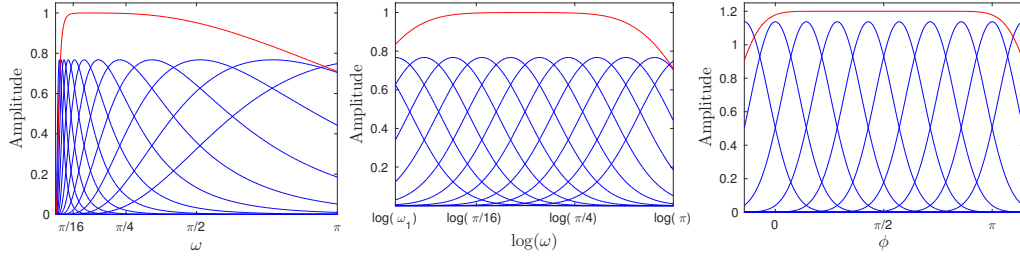


**Fig. 2.1.** LEFT: The log-normal bandpass filter bank with  $\omega_1 = \pi/50$  and  $c = 1.5$  defining the parameter values (2.3). CENTER: Summing up the filter responses enables almost uniform detection of spectral signal support within the interval  $\omega \in [\frac{\pi}{16}, \frac{\pi}{4}]$ , cf. (2.4). RIGHT: The angular part  $\hat{g}_j(\phi)$  defined by (2.5) also provides a partition of unity within the interval  $\phi \in [0, \pi]$ .

Fig. 2.1 illustrates this filter bank and also shows that it approximately provides a partition of unity of the frequency range of interest,

$$\sum_{i \in [12]} \hat{g}_i(\omega) \approx \text{constant}, \quad \text{for } \omega \in \left[ \frac{\pi}{16}, \frac{\pi}{4} \right]. \quad (2.4)$$

In particular, very low frequencies and the global mean value of a signal, to which these filters are applied, are suppressed, as is the high-frequency range  $\omega > \frac{\pi}{2}$  which is likely to be dominated by noise under realistic imaging conditions.

**Extension to 2D.** The extension of (2.1) to 2D reads

$$\begin{aligned} \hat{g}_{i,j}(\omega) &= \frac{\omega_i}{\|\omega\|} \hat{g}_i(\|\omega\|) \hat{g}_j(\phi) = \\ &= \frac{1}{C(\sigma_i) C(n_\phi)} \left( \frac{\omega_i}{\|\omega\|} \right)^2 \exp \left[ -\frac{1}{2} \left( \frac{\log(\frac{\|\omega\|}{\omega_i})}{\sigma} \right)^2 \right] \cos \left( \frac{\phi - \phi_j}{2} \right)^{2n_\phi}, \end{aligned} \quad (2.5)$$

$$(2.6)$$

with polar coordinates  $\omega = (\omega_1, \omega_2) \mapsto (\|\omega\|, \phi)$  on the right hand side and parameters: center frequency  $\omega_i$ , frequency width  $\sigma$ , center angle  $\phi_j$ , parameter  $n_\phi \in \mathbb{N}$  and  $C(n_\phi) = \frac{2\pi}{2^{2n_\phi}} \binom{2n_\phi}{n_\phi}$ . In comparison to the one-dimensional case (2.1), this filter consists of a radial and an angular part. This *separability* is relevant for implementations of the filter in the spatial domain as convolution operators. The angular part yields orientation-selective filters whose selectivity

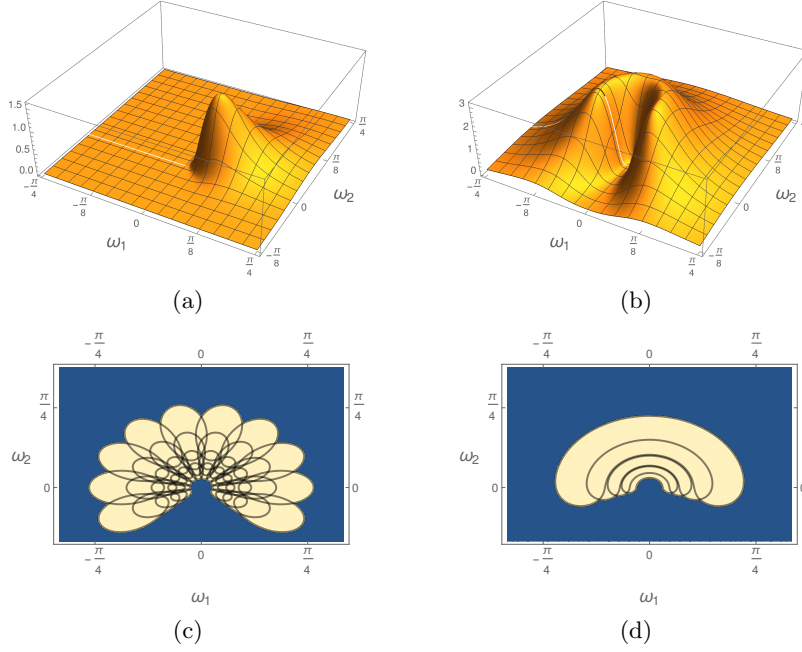


**Fig. 2.2.** (a) Two dimensional log-normal filter defined by (2.5) for  $i = 6$ ,  $j = 2$ . (b) The composed log-normal filter  $G_i(\omega)$  given by (2.11) illustrates the contribution of all filters at a single center frequency to the entire angular range. (c) Contours of log-normal filters illustrate the self-similar design and the partition of unity. (d) Contours of the composed log-normal filters used as a filter bank for our application.

can be tuned by selecting  $n_\phi$ . In connection with the filter parameters (2.3), we fixed  $n_\phi = 16$ .

Fig. 2.2 (c) illustrates the filters  $\{\hat{g}_{i,j}(\omega)\}$  corresponding to the parameters (2.3), with additional center angles  $\phi_j$  given by

$$\phi_j = (j - 1) \frac{\pi}{7}, \quad j \in \{0, 1, \dots, 9\}. \quad (2.7)$$

**Extension to 3D.** In spherical coordinates  $\omega = (\omega_1, \omega_2, \omega_3) \mapsto (\|\omega\|, \theta, \phi)$ , our three-dimensional version of the log-normal filter reads

$$\hat{g}_{i,j,k}(\omega) = \left( \frac{\omega_i}{\|\omega\|} \right)^2 \hat{g}_i(\|\omega\|) \hat{g}_j(\phi) \hat{g}_k(\theta) = \quad (2.8)$$

$$\frac{1}{C} \left( \frac{\omega_i}{\|\omega\|} \right)^3 \exp \left[ -\frac{1}{2} \left( \frac{\log(\frac{\|\omega\|}{\omega_i})}{\sigma} \right)^2 \right] \cos \left( \frac{\phi - \phi_j}{2} \right)^{2n_\phi} \cos \left( \frac{\theta - \theta_k}{2} \right)^{2n_\theta}, \quad (2.9)$$

with the normalizing factor  $C = C(\sigma)C(n_\phi)C(n_\theta)$ ,  $C(n_\phi) = C(n_\theta)$  and  $n_\phi = n_\theta$ . The center values of the additional angular variable are

$$\theta_k = (k - 1) \frac{\pi}{7}, \quad k = 1, \dots, 8. \quad (2.10)$$

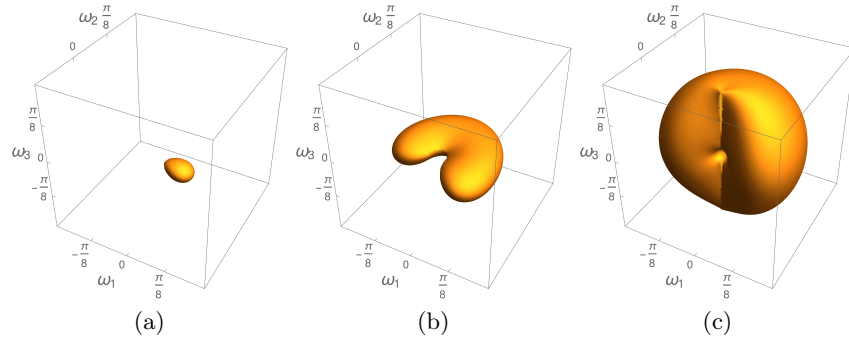


**Fig. 2.3.** In figure (a) we illustrate the extension of the 2D filter to 3D defined by (2.8) for the parameters  $i = 7$ ,  $j = 1$  and  $k = 5$ . (b)  $\sum_j \hat{g}_{i,j,k}(\omega)$  for fixed  $i = 7$  and  $k = 5$ . (c)  $G_i(\omega) = \sum_{j,k} \hat{g}_{i,j,k}(\omega)$  for fixed  $i = 7$  (cf. (2.11)).

Fig. 2.3 illustrates the resulting filters. The proposed filter bank is designed to "see" the flow in all directions (in view of turbulent flow scenarios) and to be independent of the orientation angle. For this reason we sum up several filters along the angular parameters and consider the remaining radial component  $\omega_i$  as the only filter parameter.

**Spatio-Temporal Filter Bank.** The filter bank is parametrized by the finite set of center frequency values  $\omega_i$  and defined by

$$\hat{G}_i(\omega) = \sum_j \hat{g}_{i,j}(\omega) \quad (\text{in 2D}) \quad \text{and} \quad \hat{G}_i(\omega) = \sum_{j,k} \hat{g}_{i,j,k}(\omega), \quad (\text{in 3D}) \quad (2.11)$$

where  $\hat{g}_{i,j}(\omega)$  and  $\hat{g}_{i,j,k}(\omega)$  are given by (2.5) and (2.8), respectively. The parameters are listed in (2.3), (2.7), (2.10).

### 3 Local Flow Estimation

For an image sequence  $f(x, t)$ , the response function of a filter  $G_i$  (2.11) reads

$$h_i(x, t) = (f * G_i)(x, t) = \mathcal{F}^{-1}(\hat{f} \cdot \hat{G}_i)(x, t) = r_i(x, t)e^{i\psi_i(x, t)}, \quad (3.1)$$

with the amplitude function  $r_i(x, t) = |h_i(x, t)|$  and the phase function

$$\psi_i(x, t) = \arg(h_i(x, t)) = \Im(\ln(h_i(x, t))) \in (-\pi, \pi]. \quad (3.2)$$

The basic assumption underlying local motion estimation is that *phase functions*  $\psi_i(x, t)$  are *approximately conserved under motion*, that is

$$\frac{d}{dt}\psi_i = \langle \nabla \psi_i(x, t), (\dot{x}, 1) \rangle = \langle \nabla_x \psi_i(x, t), \dot{x} \rangle + \partial_t \psi_i(x, t) \approx 0, \quad \forall(x, t). \quad (3.3)$$

As a result, after estimating the partial derivatives of all functions  $\psi_i$ , we estimate the velocity  $v = \dot{x}$  for any fixed space-time point  $(x, t)$  by minimizing the squared residual error of the latter equation, namely

$$u(x, t) = \arg \min_v \sum_i (\langle \nabla_x \psi_i(x, t), v \rangle + \partial_t \psi(x, t))^2. \quad (3.4)$$

**Estimating the partial derivatives of  $\psi(x, t)$ .** We express the partial derivatives  $\nabla \psi$  by partial derivatives of a *smooth* signal  $h$ , as follows

$$h = r e^{i\psi}, \quad \nabla h = (\nabla r) e^{i\psi} + (r e^{i\psi}) (\mathbf{i} \nabla \psi) = e^{i\psi} \nabla r + \mathbf{i} h \nabla \psi \quad (3.5a)$$

$$\nabla \psi = \frac{1}{|h|^2} \Im(\bar{h} \nabla h), \quad \bar{h} \nabla h = r e^{-i\psi} \nabla h = r \nabla r + \mathbf{i} |h|^2 \nabla \psi. \quad (3.5b)$$

We numerically estimate the partial derivatives of  $\nabla h$  by separable 3D filters whose frequency response are obtained by an orthogonal expansion of the desired behaviour in the Fourier domain (derivative filter at low frequencies, noise suppression at high frequencies) using Krawtchouk polynomials [8, 22]. These filters are similar to derivative-of-Gaussian filters but avoid aliasing artefacts in the case of filters with small spatial support, that would result from merely sampling the continuous impulse response.

## 4 Experimental Results

In Section 4.1 we report synthetic experiments for ‘1D videos’ that validate and illustrate the filter bank design, followed by 2D pipe flow scenarios in Sections 4.2 and 4.3, including real in-vitro data in laminar and turbulent flow scenarios.

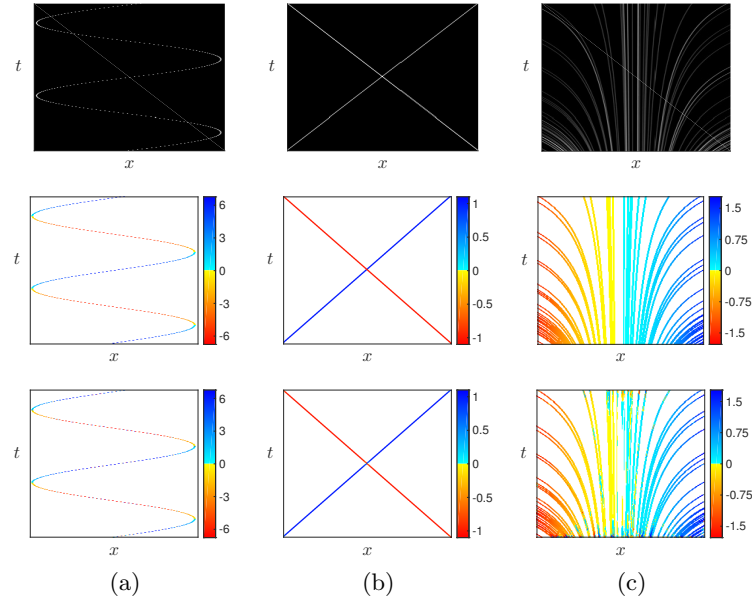
### 4.1 One-Dimensional Synthetic Ground Truth Videos

We illustrate the filter characteristics for the following 1D scenarios:

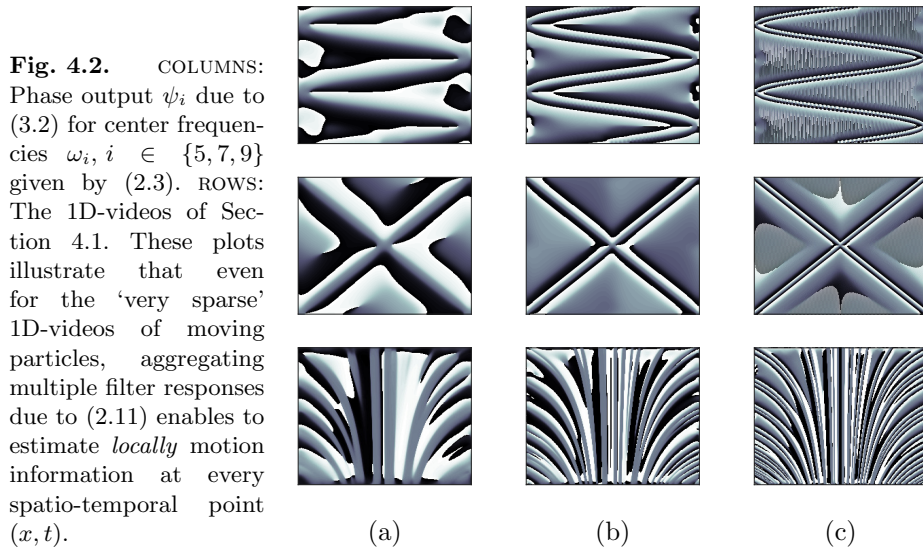
- (a) Harmonic oscillation of a single particle,  $x(t) = a \sin(\omega t)$ , with oscillation amplitude  $a > 0$  and angular frequency  $\omega > 0$ .
- (b) Elastic collision of two point particles that move with constant velocities.
- (c) Flow of multiple particles with velocities

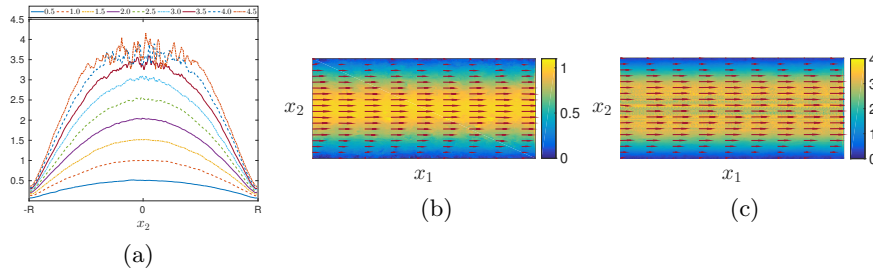
$$\dot{x} = v(x) = \begin{cases} -\alpha x^2, & x \leq 0 \\ \alpha x^2, & x > 0 \end{cases}, \quad \alpha > 0. \quad (4.1)$$

Fig. 4.1 and 4.2 illustrate the videos in terms of space-time trajectories of the particles and their velocities, and the phase functions of the aggregated complex filter responses (2.11). Due to the smoothness of these functions, velocity estimates are accurate even though moving particles cause sharp intensity changes in the spatio-temporal domain.



**Fig. 4.1.** TOP ROW: Space-time trajectories for the 1D videos of Section 4.1. CENTER ROW: Ground truth velocities. BOTTOM ROW: Estimated velocities for the harmonic oscillator (a), the elastic collision of two particles (b) and for the flow of multiple particles (c), using the phase functions displayed by Fig. 4.2. These estimates are accurate except for small regions close to the boundaries in trajectory direction, that exhibit natural errors caused by overlapping filter supports.





**Fig. 4.3.** (a) Estimates of time-averaged velocity profiles for several peak velocities  $v_m$ . The parabolic profile is well reconstructed if  $v_m < 3$ . For  $v_m \geq 3$ , motion-induced temporal frequencies cause aliasing effects (cf. [2, Section 2.2.3]) at the center of the tube, which could be fixed by spatial subsampling. Fig. (b) and (c) illustrate the accurately estimated time-averaged velocity fields for  $v_m = 1$  and  $v_m = 4$ , respectively.

## 4.2 Laminar Pipe Flow: Ground Truth Data

We validated the proposed method in 2D using synthetic image sequences of uniformly distributed point-particles, driven the laminar pipe flow in (1.1). We generated a spatial-temporal dataset of size  $256 \times 256 \times 256$  with peak velocities  $v_m \in \{0.5, 1, \dots, 4, 4.5\}$  pixels/frame. We estimated the velocity field by minimizing (3.4) using the 3D filter bank in (2.11). The results are shown in Fig. 4.3.

## 4.3 Ultrasound Particle Image Velocimetry: In Vitro Data

Fig. 4.4 depicts *real* in vitro *flows* for both a *laminar* and a *turbulent* scenario, along with time-averaged local flow estimates  $\hat{u}(x^{(k)}) = (\hat{u}_1(x^{(k)}), \hat{u}_2(x^{(k)}))^\top$  based on (3.4) and parameter estimates  $v_m, N$  of the flow model (1.2). The in vitro plane wave ultrasound experiments imaging the flow in a pipe of a fluid seeded with air bubbles were performed under controlled conditions [20]. The relevant experimental parameters include: image acquisition rate  $f = 6.66$  kHz, fluid density  $\rho = 1038$  kg/m<sup>3</sup>, viscosity  $\mu = 4.1$  mPa·s, radius of the pipe  $R = 5$  mm, field of view  $21.3 \times 37.8$  mm<sup>2</sup>, image size  $288 \times 384$  and number of temporal frames 298. We obtained parameter estimates  $v_m, N$  by minimizing the objective

$$f(v_m, N) = \sum_k \|\hat{u}(x^{(k)}) - R(\vartheta)u(x^{(k)}; v_m, N)\|^2, \quad v_m \geq 0, N \geq 1, \quad (4.2)$$

where the rotation matrix  $R(\vartheta)$  accounts for the tilted pipe (indicated by the dashed lines in Fig. 4.4) and  $u(x^{(k)}; v_m, N)$  is given by (1.2).

The sum runs over all image points  $x^{(k)}$  contained in the interior of the tube. The minimization problem was solved using the spectral projected gradient method [3] using the default parameters specified by the authors and with the non-monotone parameter value  $M = 2$ . The initial values for  $v_m$  and  $N$  were randomly chosen in the intervals  $(0, 2)$  and  $(1, 4)$ , respectively. The program was

	$Q$ [m <sup>3</sup> /s]	Re	$v_m$	$N$	$v_{(ave)}$	$v_{(ave)}^*$
laminar flow	$15 \cdot 10^{-6}$	484	0.356	1.361	0.193	0.295
turbulent flow	$80 \cdot 10^{-6}$	2579	1.557	3.547	1.081	1.577

**Table 1. In vitro ultrasound experiments.** Relevant parameters: volume flow rate  $Q$ , measured with a flow-meter, and Reynolds number Re. Estimated parameters (cf. (1.2)):  $v_m$ ,  $N$ ; relation to the average velocity  $v_{(ave)} = v_m(N + 1)/(N + 3)$ ; independent reference value for the average velocity:  $v_{(ave)}^* = Q/(\pi R^2)$ . The velocities are given in pixels/frame.

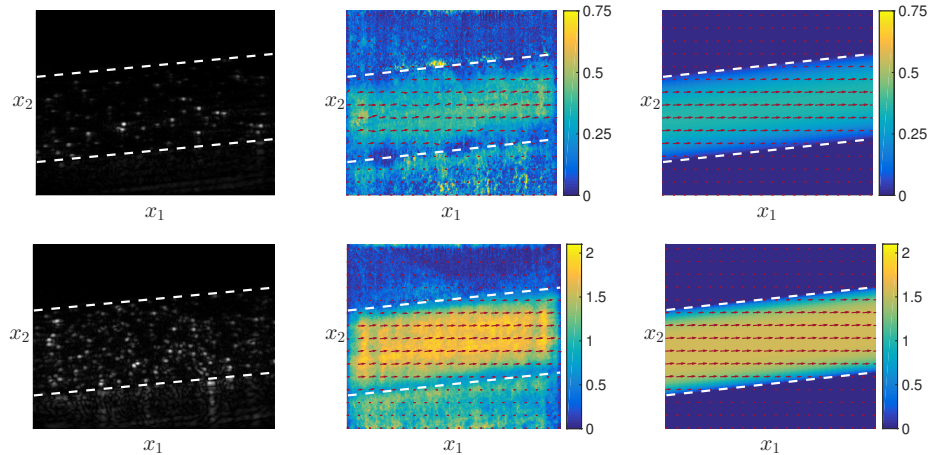


**Fig. 4.4. In vitro data.** TOP ROW: laminar steady flow. BOTTOM ROW: turbulent flow. LEFT: image sequence. CENTER: time-averaged local flow estimate. RIGHT: flow model estimate. Table 1 reports quantitative results.

stopped after 10 iterations. The estimated velocity fields depicted by Fig. 4.4 and the quantitative results in Table 1 show that our method achieves realistic estimates. The reference value  $v_{(ave)}^*$  is calculated from the volume flow rate  $Q$  that was measured during the experiment.

## 5 Conclusion

We presented an efficient approach to flow parameter estimation using plane wave ultrasound image sequences. The method achieves realistic estimates in laminar and turbulent scenarios. We consider it as a first step towards adapting techniques from computer vision to Echo PIV, to provide an alternative to the prevailing correlation methods. Future work will reconsider (i) the image reconstruction methods that lead to Echo PIV image sequences, (ii) refine our local spatio-temporal approach based on a more detailed flow representation in Fourier space, and (iii) integrate both lines of research into a variational model.

## References

1. Adelson, E.H., Bergen, J.R.: Spatiotemporal Energy Models for the Perception of Motion. *J. Opt. Soc. Am. A* 2(2), 284–299 (1985)
2. Becker, F., Petra, S., Schnörr, C.: Optical Flow. In: Scherzer, O. (ed.) *Handbook of Mathematical Methods in Imaging*, pp. 1945–2004. Springer, 2nd edn. (2015)
3. Birgin, E.G., Martinez, J.M., Raydan, M.: Nonmonotone Spectral Projected Gradient Methods on Convex Sets. *SIAM J. OPTIM* 10(4) (2000)
4. Bodnariuc, E., Schiffner, M., Petra, S., Schnörr, C.: Plane Wave Acoustic Superposition for Fast Ultrasound Imaging. In: *International Ultrasonics Symposium (IUS)*. IEEE (2016)
5. Correia, M., Provost, J., Tanter, M., Pernot, M.: 4D Ultrafast Ultrasound Flow Imaging In Vivo Quantification of Arterial Volumetric Flow Rate in a Single Heartbeat. *Physics in Medicine & Biology* 61(23), L48–L61 (2016)
6. Fleet, D., Jepson, A.: Computation of Component Image Velocity from Local Phase Information. *Int. J. Comp. Vision* 5(1), 77–104 (1990)
7. Haglund, L.: Adaptive Multidimensional Filtering. Ph.D. thesis, Dept. Electrical Engineering, University of Linköping, Sweden (1992)
8. Hashimoto, M., Sklansky, J.: Multiple-Order Derivatives for Detecting Local Image Characteristics. *Computer Vision, Graphics, and Image Understanding* 39, 28–55 (1987)
9. Heeger, D.: Optical Flow Using Spatiotemporal Filters. *Int. J. Comp. Vision* 1(4), 279–302 (1988)
10. Heitz, D., Mémin, E., Schnörr, C.: Variational fluid flow measurements from image sequences: synopsis and perspectives. *Exp. Fluids* 48(3), 369–393 (2010)
11. Kim, H., Hertzberg, J., Shandas, R.: Development and Validation of Echo PIV. *Exp. Fluids* 36(3), 455–462 (2004)
12. Leow, C.H., Bazigou, E., Eckersley, R.J., Yu, A.C.H., Weinberg, P.D., Tang, M.X.: Flow Velocity Mapping Using Plane Wave Ultrasound Imaging. *Ultrasound in Medicine and Biology* 41(11), 2913–2925 (2015)
13. Margarey, J., Kingsbury, N.: Motion Estimation Using a Complex-Valued Wavelet Transform. *IEEE Trans. Signal Proc.* 46(4), 1069–1084 (1998)
14. Massot, C., Héroult, J.: Model of Frequency Analysis in the Visual Cortex and the Shape from Texture Problem. *Int. J. Comp. Vision* 76(2), 165–182 (2008)
15. Poelma, C.: Ultrasound Imaging Velocimetry: a review. *Exp. Fluids* 58(1), 3–31 (2017)
16. Raffel, M., Willert, C.E., Wereley, S.T., Kompenhans, J.: *Particle Image Velocimetry – A Practical Guide*. Springer (2007)
17. Simoncelli, E., Freeman, W., Adelson, E., Heeger, D.: Shiftable Multiscale Transforms. *IEEE Trans. Inf. Theory* 38, 587–607 (1992)
18. Stigler, J.: Analytical Velocity Profile in Tube for Laminar and Turbulent Flow. *Engineering Mechanics* 21(6), 371–379 (2014)
19. Tanter, M., Fink, M.: Ultrafast Imaging in Biomedical Ultrasound. *IEEE Transactions on Ultrasonics, Ferroelectrics, and Frequency Control* 61(1), 102–119 (2014)
20. Voorneveld, J., Kruizinga, P., Vos, H.J., Gijzen, F.J.H., Jebbink, E.G., van der Steen, A.F.W., de Jong, N., Bosch, J.G.: Native Blood Speckle vs Ultrasound Contrast Agent for Particle Image Velocimetry with Ultrafast Ultrasound - in Vitro Experiments. In: *International Ultrasonics Symposium*. IEEE (2016)
21. White, F.M.: *Fluid Mechanics*. McGraw-Hill Series in Mechanical Engineering, McGraw Hill, New York (2011)

12 Ecaterina Bodnariuc, Stefania Petra, Christoph Schnörr, Jason Voorneveld

22. Yap, P.T., Paramesran, R., Ong, S.H.: Image Analysis by Krawtchouk Moments. IEEE Transactions on Image Processing 12(11), 1367–1377 (Nov 2003)